RSC Advances

PAPER

View Article Online
View Journal | View Issue

Cite this: *RSC Adv.*, 2022, **12**, 30976

A wrinkled nanosurface causes accelerated protein unfolding revealing its critical role in nanotoxicity†

Yuezheng Li,[a] Baoyu Li,*[b] Yang Liu,[c] Yuanyuan Qu,[c] Jian Tian*[a] and Weifeng Li*[c]

Wrinkles are often found to have a strong influence on the properties of nanomaterials and have attracted extensive research interest. However, the consequences of the use of wrinkled nanomaterials in biological systems remain largely unknown. Here, using molecular dynamics simulations, we studied the interactions of a wrinkled graphene with proteins, using the villin headpiece (HP35) as the representative model. Our results clearly revealed that the wrinkle, especially the wrinkle corner, showed stronger binding affinity to HP35 than the planar surface where HP35 experienced accelerated and more severe unfolding. This is because the transverse translocation of the aromatic residues of the protein is highly confined at the wrinkle corner. The movement of other parts of the protein causes unfolding of the protein secondary structure and releases hydrophobic residues to bind to graphene, causing complete denaturation. Further free energy analyses revealed that this is attributed to the stronger binding affinity of residues to the wrinkle corner than to the planar surface. The present findings provide a deeper understanding of the effect of graphene wrinkles on protein stability. This finding may be generalized to other types of biomolecules and may also guide the design of biomedical nanomaterials through surface structural engineering.

Received 1st September 2022
Accepted 14th October 2022

DOI: 10.1039/d2ra05489b

rsc.li/rsc-advances

1. Introduction

In the past decades, nanomaterials especially carbon-based species (including graphene, fullerene, carbon nanotubes, *etc.*) have attracted great research interest.[1–7] Because of their exceptional physical and chemical properties, they find extensive applications in the biological and medical-related fields, such as bioimaging, biosensing, drug delivery and therapeutic agents.[8–18] Meanwhile, growing concerns about the biosafety or toxicity of the nanomaterials to biological systems have also attracted considerable attention. It has been reported that carbon nanotubes can be inhaled from the air and reach the subpleural tissue.[19] Furthermore, numerous works have reported that nanomaterials can accumulate in cytoplasm, causing lung insult, immunologic toxicity and adverse cardiovascular effects.[20–24] To probe the bio-effect of the nanomaterials at the molecule level, through experimental and theoretical approaches, the interactions of nanomaterials with biomolecules (such as proteins, nucleic acids and cell membranes) have been extensively studied to address the effect of nanomaterials on the biomolecule structures.[25–30]

During the production of nanomaterials, wrinkles are commonly observed either prepared by chemical vapor deposition (CVD) or micromechanical exfoliation.[31] The existence of wrinkles can cause lattice deformation and thus induce strain in the deformed area, resulting in many interesting physical and chemical properties. For instance, the wrinkle induced strain can induce interesting quantum phenomena. Many studies have predicted that the gradient strain cause gauge field which leads to the formation of pseudo-Landau levels.[31–36] Moreover, the local curvature induced by wrinkles can significantly affect the charge-transport behavior and enhance the chemical reactivity of graphene.[37,38] It has also been demonstrated that the wrinkled structures can improve the stretchability of graphene-based flexible electronic devices.[39,40] Despite the enormous research interests of graphene materials in biological and medical applications, the consequence of the wrinkled structures on the biological effects is largely unknown. Many previous works have shown that the morphology of nanomaterials did have significant influence on their biological performances such as cellular uptake, biodistribution and blood circulation durations.[41–43] More importantly, given the increasing prevalence of nanomaterials applied to biomedical fields, the systematic understanding of the influence of wrinkles on biomolecules structures surely deserves more effects to guide future experimental studies.

[a]*School of Materials Science and Engineering, Shandong University of Science and Technology, Qingdao 266590, China. E-mail: jiantian@sdust.edu.cn*

[b]*School for Radiological and Interdisciplinary Sciences (RAD-X), Collaborative Innovation Center of Radiation Medicine of Jiangsu Higher Education Institutions, Soochow University, Suzhou 215123, China. E-mail: byli@suda.edu.cn*

[c]*School of Physics, Shandong University, Jinan 250100, China. E-mail: lwf@sdu.edu.cn*

† Electronic supplementary information (ESI) available. See DOI: https://doi.org/10.1039/d2ra05489b

In this work, we systematically explored the interaction process of wrinkled graphene (abbreviated as W-Gra in the following discussions) with protein using a widely adopted protein model (villin headpiece HP35) by all-atom molecular dynamics (MD) simulations. Graphene nanosheet with ideal planar surface (ideal graphene, abbreviated as I-Gra) was used as control. Our data reveals that both W-Gra and I-Gra can attract HP35 and form stable binding. Notably, the HP35 experiences severe structural deformation after binding to W-Gra. Additionally, we find that the transverse translocation of residues is highly confined at the wrinkle corner and migrate along it. In contrast, on I-Gra, HP35 can well maintain its native structure for a relatively longer time. Our present findings elucidate the importance of graphene wrinkle on the interactions with biomolecules.

2. Simulation methods

2.1 All-atom MD simulations

The initial structure of the chicken villin headpiece subdomain protein (HP35) was obtained from the Protein Data Bank (PDB code: 1YRF (ref. 44)) and modeled by CHARMM27 force field.[45] We selected HP35 as the representative model protein because its folding and unfolding kinetics have been well documented in experimental and theoretic studies.[46–49] The W-Gra nanosheet model consists 3600 carbon atoms with a dimension of 9.89 × 8.80 nm^2, while the I-Gra nanosheet consists 1500 carbon atoms with a dimension of 6.14 × 6.38 nm^2. Following experimental observations,[50–54] we have constructed a wrinkle model with a width of 2.99 nm and height of 0.98 nm as shown in Fig. 1A and B. Additionally, the main findings were verified by a larger winkle with a larger height of 1.77 nm (data were shown in ESI Materials†) which gave consistent results. The carbon atoms of two graphene models were modeled as uncharged Lennard–Jones particles with a cross section of σ_{cc} = 0.34 nm and a potential well depth of ε_{cc} = 0.36 kJ mol^{-1}.[55] In the simulations, the HP35 protein was initially placed above the W-Gra/I-Gra nanosheet with a minimum distance of 2.44 nm as shown in Fig. 1C. Then they were solvated in a water box with periodic boundary conditions in all three directions. The TIP3P water model[56] was used and two Cl^- atoms were added to neutralize the net charge of HP35. Detailed information about two simulation systems is summarized in Table 1.

Table 1 The configurations of two simulation models

	HP35–W-Gra	HP35–I-Gra
Box size (nm^3)	9.89 × 8.80 × 8.00	6.14 × 6.38 × 6.00
Number of water	21 479	6995
Number of ions	$2Cl^-$	$2Cl^-$

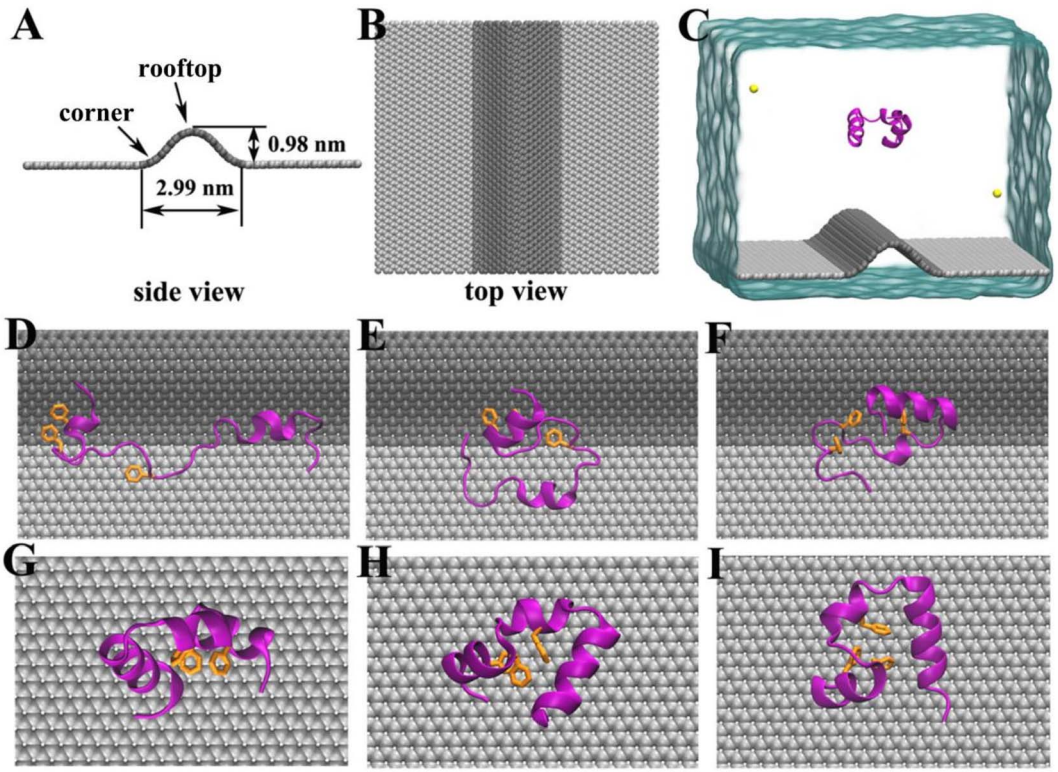

Fig. 1 (A) Side view and (B) top view of the graphene nanosheet with a wrinkle; the carbon atoms in the wrinkled area are shown as dark gray spheres while the others are shown as light gray spheres. (C) The initial system where the HP35 protein is shown in ribbon representation, chlorine ions are shown as yellow spheres and water box is rendered as a cyan surface. The final structures of HP35 adsorbed onto (D–F) W-Gra and (G–I) I-Gra surface after 500 ns simulation respectively. The hydrophobic core formed by three phenylalanine (Phe 6, 10, and 17) is shown as orange sticks.

All simulations were conducted using the GROMACS package (version 4.6.6).[57] All the bonds involving hydrogen atoms were maintained with the LINCS algorithm.[58] The electrostatic interactions were treated using the particle mesh Ewald (PME) method[59,60] (the maximum Fourier spacing for the FFT gird is 0.1 nm and the electrostatic energy tolerance is 1×10^{-5}), while van der Waals interactions were calculated with a cutoff distance of 1.0 nm. All the carbon atoms in two models were fixed during the simulations. After energy minimization, all models were equilibrated for 500 ps in the NVT ensemble using v-rescale thermostat[61] at 300 K. Then, 500 ns simulations were conducted for data production at a constant pressure of 1 bar and a temperature of 300 K using the Berendsen coupling method.[62] Three independent trajectories for each model were generated, yielding a total simulation time of 3 μs.

2.2 Potential of mean force (PMF) calculations

To quantitatively describe the adsorption strength between HP35 and two graphene models, the potential of mean force (PMF) values of the HP35 pulling from the W-Gra or I-Gra surfaces were calculated along the z-direction using the umbrella sampling method.[63] Technically, the distance (d) of HP35 to the W-Gra or I-Gra surface was restrained at a reference distance (d_0) with a harmonic force

$$F = k \times (d - d_0)$$

where k is the force constant (ranging from 2000 to 20 000 kJ mol^{-1} nm^{-2}). The resolution of the distance was 0.05 nm. In the calculation, the d was chosen from 0 (the firmly binding conformation) to 1.7 nm (totally separated conformation). At each d_0, the system was equilibrated for 2 ns followed by 10 ns productive simulation. The PMF profiles were obtained by the g_wham tool that implements the Weighted Histogram Analysis Method.[64,65]

3. Results and discussion

3.1 Binding process of HP35 to two graphene models

In our simulations, the initial separation between HP35 and W-Gra/I-Gra surfaces was 2.24 nm as shown in Fig. 1C. During the simulation, we observed that HP35 freely dissolved in water for several nanoseconds, then adsorbed onto W-Gra/I-Gra in all trajectories. Notably, the HP35 was found to interact with two graphene models with distinct binding patterns. For the HP35 with W-Gra, clear structural distortions were observed for HP35 in 500 ns simulations. The native conformation of HP35 consists of three α-helical segments and a hydrophobic core formed by three phenylalanine (Phe 6, 10, and 17). As depicted in Fig. 1D–F, some of the α-helical segments of HP35 unfolded and the hydrophobic core which is important for maintaining protein's stability was also destroyed. In contrast, for the I-Gra simulations, the native structure of HP35 was well maintained after the adsorption onto I-Gra surface and no obvious distortion or unfolding events were detected after 500 ns simulations (Fig. 1G–I). In a previous study of the binding process of double-stranded DNA (dsDNA) with wrinkled graphene,[66] we also noticed that dsDNA experiences severe structural deformation upon binding to a wrinkled graphene surface, whereas it tends to maintain its native structure upon binding to an idealized graphene nanosheet. Thus, the denaturing behavior of the wrinkle in nanomaterials to bio-molecules could be an inherent character that should be pay more attentions when utilized in biological and medical areas.

From the simulation traj-1, we took some representative snapshots at various times to show the specific unfolding

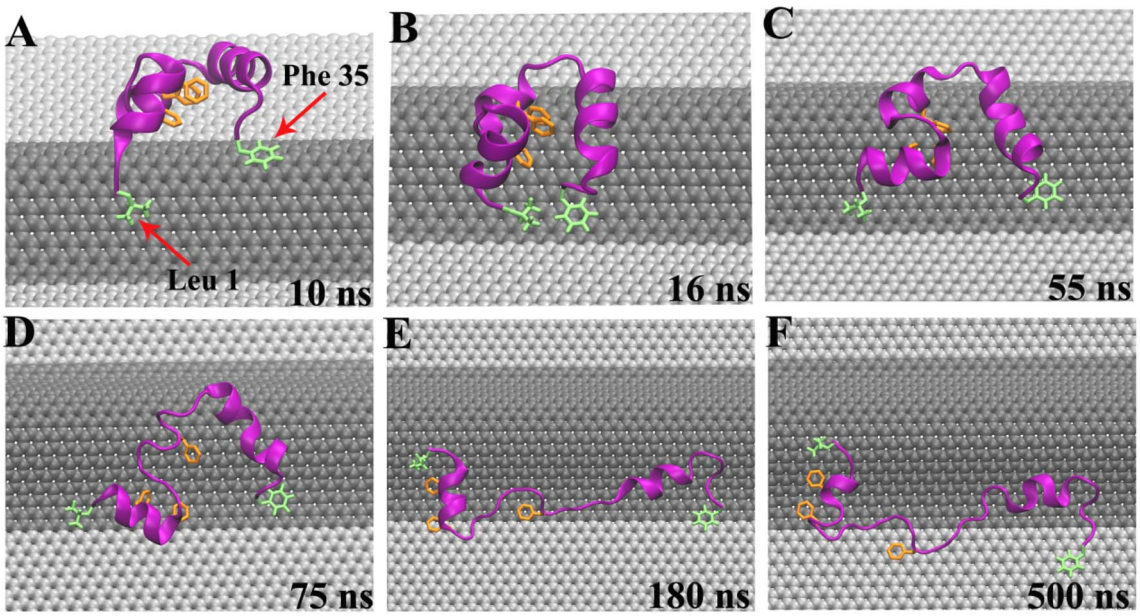

Fig. 2 Structural evolutions of HP35 on W-Gra surface in a representative trajectory. The hydrophobic core of HP35 is shown as orange sticks. The residues Leu 1 and Phe 35 that play important role in the unfolding process are shown as lime sticks.

process of HP35 on W-Gra surface (Fig. 2). At $t = 10$ ns, HP35 loaded to W-Gra nanosheet and formed direct contact with the ridge of wrinkled region through residues Leu 1 and Phe 35, as shown in Fig. 2A. After 6 ns, these two residues slid to the edge of the wrinkle (Fig. 2B) and the movements of them were restricted nearby in the following simulations (Fig. 2C). While other parts of the protein still migrated around the ridge of wrinkle, the HP35 began to unfold which initiated at the helix-2 segment (Fig. 2D). Meanwhile, the hydrophobic core of HP35 was also destroyed as displayed in Fig. 2D. The local unfolding of protein led to the expose of buried residues inside HP35 to interact with W-Gra which accelerated the protein denaturation (Fig. 2E and F). In the other trajectories, the similar trend of protein unfolding was also observed which can be found in Fig. S1 and S2 in the ESI.†

To quantitatively describe the binding processes of HP35 to W-Gra and I-Gra, we calculated the number of contacts between HP35 heavy atoms with W-Gra and I-Gra (abbreviated as N_{cont}), respectively. Here, two atoms within a separation of 0.5 nm were treated as contacted. As depicted in Fig. 3A, for the HP35–W-Gra simulations, a quick increase was observed for N_{cont} to around 40 within 15 ns, representing the initial loading stage of HP35. Then the N_{cont} gradually increased to around 80–140 from 15 ns to around 200 ns. From then on N_{cont} fluctuated during the remaining simulation, which represented the stable binding with W-Gra. In sharp contrast, for the adsorption of HP35 onto I-Gra (Fig. 3B), after the quick increase of N_{cont} to 30–40 at the initial stage, no clear increase was detected during the entire simulations, revealing the high stability of HP35 on I-Gra. The other parallel trajectories also show similar phenomenon which can be found in Fig. 2, S1 and S2.†

To probe the energetic origin of the different binding patterns of HP35 onto W-Gra and I-Gra, we then calculated the interaction energies between HP35 and two graphene models. The two systems exhibited different trends where HP35 binding to W-Gra (Fig. 3C) in much stronger strength than that with I-Gra (Fig. 3D). This is well consistent with N_{cont} profiles in Fig. 3A and B because more contacts between HP35 and W-Gra result in the stronger interactions. In contrast, the HP35 formed less contacts with I-Gra. Thus, the weaker interaction was incapable of causing structure distortions of HP35.

3.2 Structure changes of HP35 during binding

The structural changes of HP35 upon binding onto W-Gra and I-Gra were quantitatively assessed by calculating the root-mean-squared deviation (RMSD) of the heavy atoms with respect to the crystal structure and the results are summarized in Fig. 3E and F. The structure changes were found to be in line with the change of N_{cont} and interacting energy. For the system of HP35 with W-Gra, the relatively larger RMSD value and fluctuations indicated clear deformation of the HP35 structure upon binding to W-Gra. In contrast, for HP35 with I-Gra, the RMSD was small revealing that no changes happened for the HP35 structure. This is consistent with the final configurations of HP35 adsorbed onto W-Gra and I-Gra surfaces as presented in Fig. 1D–I.

From the RMSD analyses, more severe unfolding of HP35 was observed upon adsorption with W-Gra than that with I-Gra although the three trajectories show different evolutions for the structure change. For clearer comparison of structural changes of HP35 binding to W-Gra and I-Gra, we computed its secondary structure using the Define Secondary Structure of Proteins

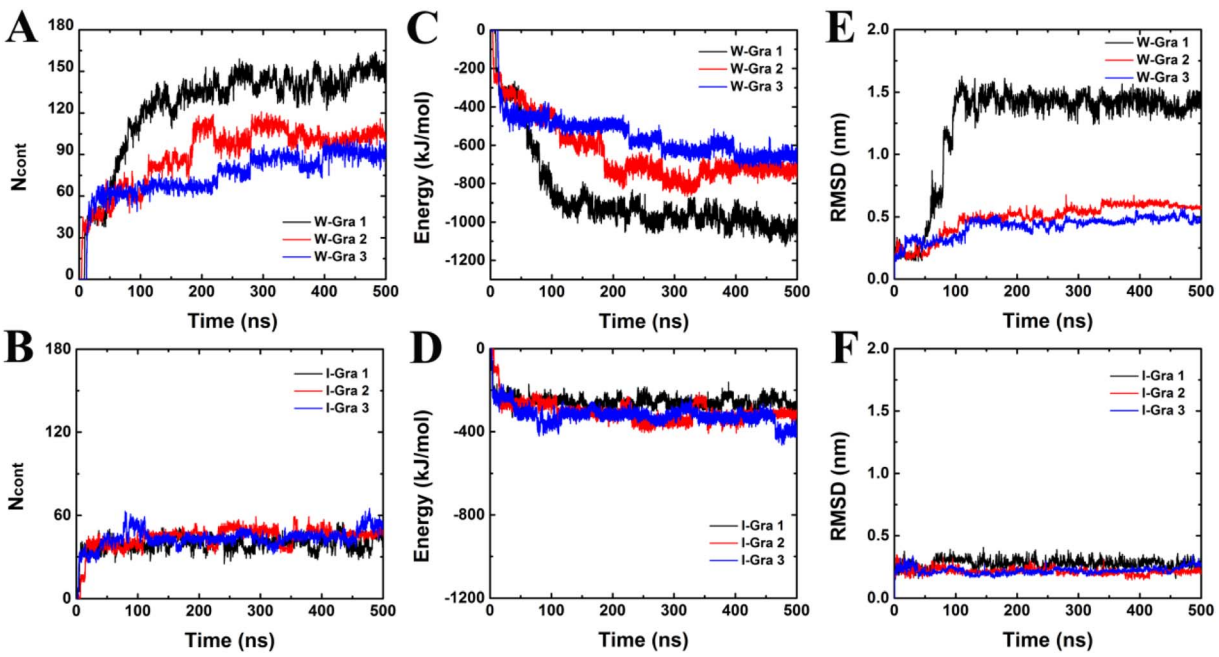

Fig. 3 Time evolutions of the contact number (N_{cont}) between HP35 heavy atoms and (A) W-Gra and (B) I-Gra. The time evolutions of interaction energy of HP35 binding to (C) W-Gra and (D) I-Gra. Time evolutions of the root-mean-squared deviation (RMSD) of the HP35 heavy atoms with respect to the crystal structure upon binding to the (E) W-Gra and (F) I-Gra. For each model, three trajectories have been conducted.

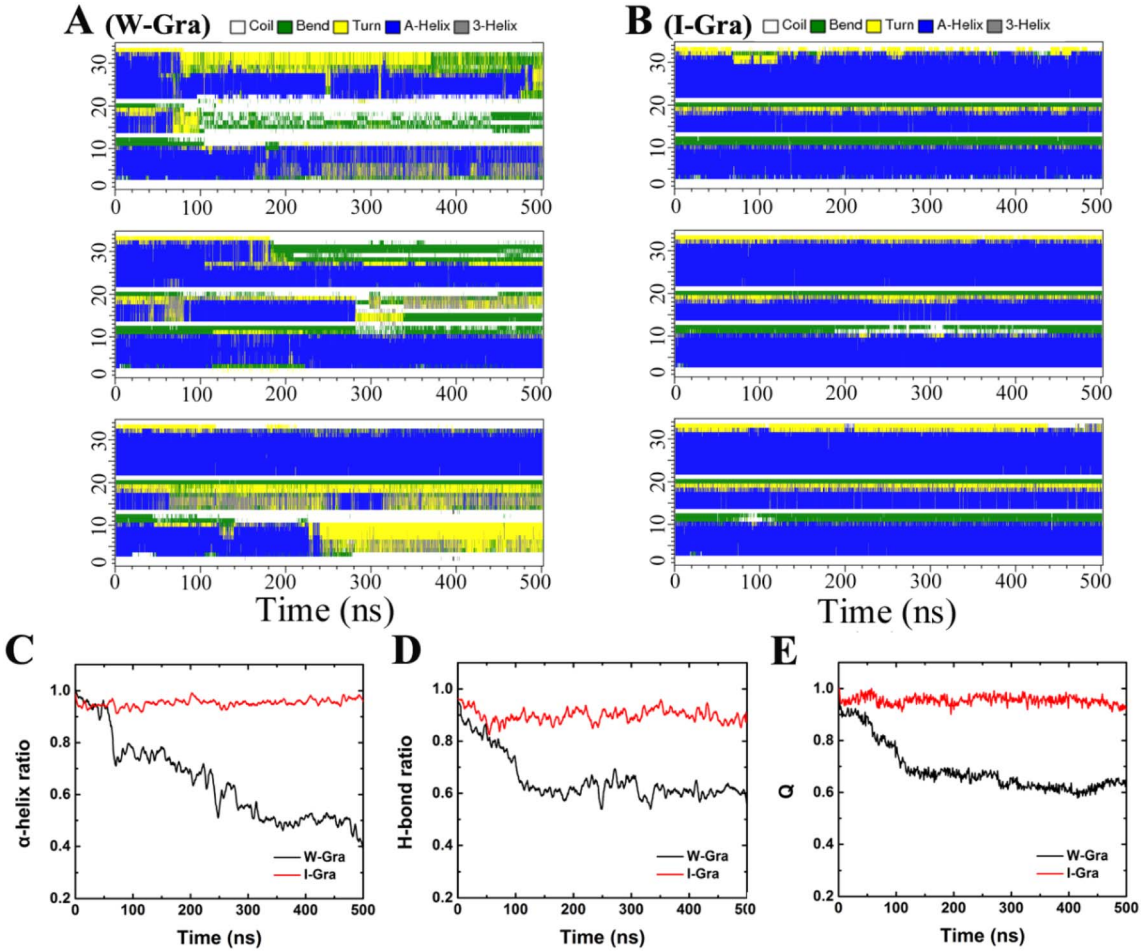

Fig. 4 Time evolutions of the secondary structure assignment of HP35 upon binding to (A) W-Gra and (B) I-Gra from three independent trajectories in each system. Time evaluations of the ratios of (C) the α-helical segment, (D) remaining hydrogen bonds and (E) native protein contacts, Q, of HP35 upon binding to the W-Gra and I-Gra. The data in (C)–(E) are averaged over the three independent trajectories.

(DSSP) program[67] implemented in the do_dssp module of Gromacs package. In the native state, HP35 has three α-helical segments: helix-1 (residues 4–10), helix-2 (residues 15–19) and helix-3 (residues 23–32). As shown in Fig. 4A, upon binding to W-Gra, the helix-2 segment in all trajectories, the helix-3 segment in traj-1 and the helix-2 segment in traj-3 unfolded completely. In contrast, all the helical segments of HP35 were largely maintained upon binding to I-Gra in three 500 ns trajectories (Fig. 4B). The residual ratios of HP35 α-helix revealed that HP35 lost around 60% and 0.4% (data averaged all trajectories) of its helical segments upon binding to W-Gra and I-Gra, respectively (Fig. 4C). It is well known that the hydrogen bonds formed within the protein play a vital role in maintaining the protein secondary and tertiary structure. The structure distortion of protein is usually accompanied by broken of hydrogen bonds. To verify this, we calculated the ratio of the remaining hydrogen bonds in HP35 protein. Here, a hydrogen bond is defined as the distance between the donor–acceptor atoms less than 0.35 nm and the angle defined by the donor–hydrogen–acceptor atoms less than 30°. As shown in Fig. 4D, HP35 lost around 40% of the hydrogen bonds in contacting with the W-Gra. For comparison, only ~10% of the hydrogen bonds were broken in the I-Gra simulations. This result was well consistent with the above structure analyses where distortions of HP35 binding to W-Gra were much severer than that to I-Gra.

In depth analysis of the tertiary structure of HP35 was also conducted by calculating the fraction of protein native contacts, $Q(t)$, which was defined as the ratio of the residual number of native contacts (using a distance cutoff of 0.5 nm) at time t with respect to the value of crystal structure. Following our previous work,[68] only residue pairs separated by at least three consecutive residues were used to calculate the contacts. As can be seen in Fig. 4E, the mean $Q(t)$ over all trajectories decreased to 0.65 after 500 ns which revealed that HP35 lost 35% of the tertiary structure when binding to W-Gra. For comparison, ~93% of native contacts were preserved for HP35 with I-Gra, indicating the strong influence of graphene wrinkle on the tertiary structure of HP35.

In the three trajectories, the specific unfolding process of HP35 on W-Gra show different characteristics. However, the main finding of severer unfolding at the W-Gra than that on I-Gra is commonly observed in all the trajectories with both the

secondary structure and the tertiary structure of HP35 being destroyed after adsorption onto wrinkle. Thus, it is safe to conclude that the curvature heterogeneity in wrinkled graphene can show toxicity by causing protein denaturation.

3.3 Verification of HP35 unfolding with large wrinkled graphene and CNT models

From above analyses, the wrinkle region of graphene is found to play a key role to cause protein denaturation. To further verify this phenomenon, we simulated the adsorption of HP35 onto graphene with a larger-sized wrinkle (the height increased to 1.77 nm as depicted in Fig. S3A†) and the results were summarized in Fig. S3 in ESI.† Similar to above observation, HP35 quickly absorbed to the wrinkled area and located as the corner of the wrinkle (Fig. S3B†). Meanwhile, HP35 lost most of its native structure during binding. More specifically, HP35 lost 40% of the hydrogen bonds in protein and around 50% of the native contacts, revealing severe distortions of its tertiary structure upon binding to large wrinkled graphene. This verifies that the wrinkled graphene surface plays a major role in HP35 unfolding.

In addition to the verification with a larger wrinkle model, the rooftop of the wrinkle is believed to be inconsequential for HP35 unfolding, albeit HP35 binding to it happens. Considering that the morphology of the rooftop part is similar to carbon nanotube (CNT). Intuitively, we simulated the interaction of HP35 with CNT which mimics the rooftop. The CNT used in current work has a chiral index (15, 15) with diameter of 2.03 nm. As summarized in Fig. S4A–C,† HP35 well maintained its native structure and no obvious distortion or unfolding events were detected after binding to CNT surface in 500 ns simulations. Moreover, most of its α-helical segments (Fig. S4D†) and hydrogen bonds (Fig. S4E†) were well maintained after binding to CNT. The mean value of $Q(t)$ averaged over three trajectories decreased to around 0.83, indicating that only slight global changes happened for the tertiary structure of HP35. According to these results, we conclude that the corner of wrinkle region plays the key role in HP35 unfolding.

3.4 Unfolding origin and potential of mean force analysis

Except for the rooftop in above discussions, the wrinkle has two corners. From the unfolding snapshots in Fig. 2, we noticed that the aromatic residues (Phe for instance) tend to bind and locate at the corner of the wrinkle, further causing the unfolding and revealing the significance of the corner in HP35 unfolding. To confirm this, in Fig. 5 we show an unfolding event of HP35 after binding to wrinkle. At 55 ns, the three helical segments and the hydrophobic core of HP35 were still well maintained (Fig. 5A). Meanwhile, Phe 35 at the C-terminus formed stable binding with the wrinkle corner of W-Gra as highlighted in Fig. 5A. The firm binding of Phe 35 at the corner lasted tens of nanoseconds and at 73.2 ns, helix-2 and a part of the helix-3 segment unfolded. The helix-1 moved away from the C-terminus, causing unfolding of the buried hydrophobic core (Phe 6, 10 and 17) which then formed direct interactions with W-Gra as shown in Fig. 5B. During this process, the separation distance between Phe 17 and Phe 6/10 greatly increased from ~0.5 nm to ~1.0 nm (Fig. 5C), indicating that the hydrophobic core of HP35 was

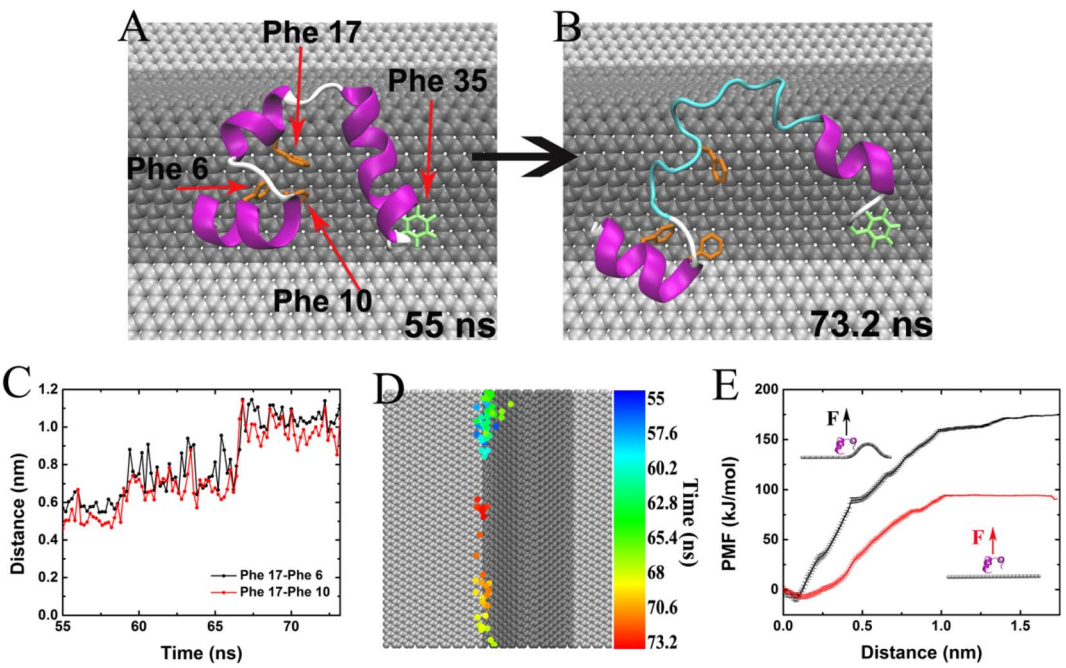

Fig. 5 (A and B) Two representative snapshots from traj-1 showing how HP35 unfolds at the wrinkle corner. (C) Time evaluation of the distance between Phe 17–6 and Phe 17–10. (D) The migration pathway of residue Phe 35 at the corner of wrinkle from 55 to 73.2 ns. (E) Potential of mean force (PMF) of HP35 binding onto the wrinkled (black) and planar (red) area of graphene.

completely destroyed. During this unfolding event, the Phe 35 is always trapped in the wrinkle corner. Fig. 5D depicts the migration pathway of Phe 35 on W-Gra surface. It's clear that the transverse migration of Phe 35 on W-Gra surface was highly confined along the corner of graphene wrinkle. Thus, the attraction strength of corner region to aromatic residues, through forming the well-known π–π interactions, is believed to be stronger than the rooftop. Such phenomenon is commonly found in other trajectories (see Fig. S5 and S6†).

To quantitatively compare the binding strength of HP35 to a wrinkled or planar graphene surface, we further calculated the binding free energies of HP35 adsorbing onto the wrinkled and planar area, respectively, by pulling HP35 away from the wrinkle corner or a planar graphene surface along the normal direction. The free energy profiles are summarized in Fig. 5E. The results clearly indicate that the binding free energy of HP35 to wrinkled area reaches abound -175 kJ mol^{-1} which is much stronger than that to planar area ($\sim$94 kJ mol^{-1}). Therefore, it is energetically advantageous for residues in HP35 protein to bind to the wrinkled area. Because the residues at the wrinkled area are highly restrained, thermal movements of other parts of the protein act to induce the unfolding process of HP35 and the exposure of inner hydrophobic residues. These residues further bind to graphene and finally results in the loss of the secondary and tertiary protein structure.

4. Conclusion

In summary, the adsorption and binding dynamics of the HP35 protein with wrinkled graphene was studies by MD simulations. We found that HP35 structure experienced severe distortions upon binding to wrinkled region on graphene. This is because of the restraints of the transverse migration of residues at the wrinkle corner was highly restrained. With the movements of the other parts of HP35, the structured domains were stretched and unfolded. By calculating free energy by umbrella sampling technique, this is because of the higher binding affinity of HP35 to the wrinkled area than that to the planar area. So, it is energetically advantageous for residues in protein to bind to the wrinkled graphene. Our present findings reveal the effect of nanomaterial wrinkle on the nano–bio interactions and provide deeper understanding of the nanotoxicity of nanomaterials.

Conflicts of interest

There are no conflicts to declare.

Acknowledgements

This work is supported by the National Natural Science Foundation of China (11874238, 51872173), Taishan Scholar Foundation of Shandong Province (No. tsqn201812068), Natural Science Foundation of Shandong Province (ZR2022JQ21) and Youth Innovation Technology Project of Higher School in Shandong Province (No. 2019KJA013).

References

1 D. K. Palit, A. V. Sapre, J. P. Mittal and C. N. R. Rao, Photophysical Properties of the Fullerenes, C-60 and C-70, *Chem. Phys. Lett.*, 1992, **195**, 1–6.
2 M. S. Dresselhaus, G. Dresselhaus and P. C. Eklund, Science of fullerenes and carbon nanotubes, *Nature*, 1996, **381**, 384.
3 K. S. Novoselov, A. K. Geim, S. V. Morozov, D. Jiang, Y. Zhang, S. V. Dubonos, I. V. Grigorieva and A. A. Firsov, Electric field effect in atomically thin carbon films, *Science*, 2004, **306**, 666–669.
4 C. Lee, X. D. Wei, J. W. Kysar and J. Hone, Measurement of the elastic properties and intrinsic strength of monolayer graphene, *Science*, 2008, **321**, 385–388.
5 S. Latil and L. Henrard, Charge carriers in few-layer graphene films, *Phys. Rev. Lett.*, 2006, **97**, 036803.
6 V. C. Sanchez, A. Jachak, R. H. Hurt and A. B. Kane, Biological Interactions of Graphene-Family Nanomaterials: An Interdisciplinary Review, *Chem. Res. Toxicol.*, 2012, **25**, 15–34.
7 J. R. Williams, L. DiCarlo and C. M. Marcus, Quantum hall effect in a gate-controlled p–n junction of graphene, *Science*, 2007, **317**, 638–641.
8 V. Krishna, A. Singh, P. Sharma, N. Iwakuma, Q. A. Wang, Q. Z. Zhang, J. Knapik, H. B. Jiang, S. R. Grobmyer, B. Koopman and B. Moudgil, Polyhydroxy Fullerenes for Non-Invasive Cancer Imaging and Therapy, *Small*, 2010, **6**, 2236–2241.
9 X. Wang, L. L. Yang, Z. Chen and D. M. Shin, Application of nanotechnology in cancer therapy and imaging, *Ca-Cancer J. Clin.*, 2008, **58**, 97–110.
10 X. M. Sun, Z. Liu, K. Welsher, J. T. Robinson, A. Goodwin, S. Zaric and H. J. Dai, Nano-Graphene Oxide for Cellular Imaging and Drug Delivery, *Nano Res.*, 2008, **1**, 203–212.
11 Y. K. Kim, H. K. Na, S. J. Kwack, S. R. Ryoo, Y. Lee, S. Hong, S. Hong, Y. Jeong and D. H. Min, Synergistic Effect of Graphene Oxide/MWCNT Films in Laser Desorption/Ionization Mass Spectrometry of Small Molecules and Tissue Imaging, *ACS Nano*, 2011, **5**, 4550–4561.
12 Z. Liu, S. Tabakman, S. Sherlock, X. L. Li, Z. Chen, K. L. Jiang, S. S. Fan and H. J. Dai, Multiplexed Five-Color Molecular Imaging of Cancer Cells and Tumor Tissues with Carbon Nanotube Raman Tags in the Near-Infrared, *Nano Res.*, 2010, **3**, 222–233.
13 H. Q. Bao, Y. Z. Pan, Y. Ping, N. G. Sahoo, T. F. Wu, L. Li, J. Li and L. H. Gan, Chitosan-Functionalized Graphene Oxide as a Nanocarrier for Drug and Gene Delivery, *Small*, 2011, **7**, 1569–1578.
14 A. A. Bhirde, V. Patel, J. Gavard, G. F. Zhang, A. A. Sousa, A. Masedunskas, R. D. Leapman, R. Weigert, J. S. Gutkind and J. F. Rusling, Targeted Killing of Cancer Cells *in Vivo* and *in Vitro* with EGF-Directed Carbon Nanotube-Based Drug Delivery, *ACS Nano*, 2009, **3**, 307–316.
15 A. Bianco, K. Kostarelos and M. Prato, Applications of carbon nanotubes in drug delivery, *Curr. Opin. Chem. Biol.*, 2005, **9**, 674–679.

16 X. Yu and M. V. Pishko, Nanoparticle-Based Biocompatible and Targeted Drug Delivery: Characterization and *in Vitro* Studies, *Biomacromolecules*, 2011, **12**, 3205–3212.
17 Y. Song, Y. N. Luo, C. Z. Zhu, H. Li, D. Du and Y. H. Lin, Recent advances in electrochemical biosensors based on graphene two-dimensional nanomaterials, *Biosens. Bioelectron.*, 2016, **76**, 195–212.
18 T. Y. Ma, Y. H. Tang, S. Dai and S. Z. Qiao, Proton-Functionalized Two-Dimensional Graphitic Carbon Nitride Nanosheet: An Excellent Metal-/Label-Free Biosensing Platform, *Small*, 2014, **10**, 2382–2389.
19 J. P. Ryman-Rasmussen, M. F. Cesta, A. R. Brody, J. K. Shipley-Phillips, J. I. Everitt, E. W. Tewksbury, O. R. Moss, B. A. Wong, D. E. Dodd, M. E. Andersen and J. C. Bonner, Inhaled carbon nanotubes reach the subpleural tissue in mice, *Nat. Nanotechnol.*, 2009, **4**, 747–751.
20 A. E. Porter, M. Gass, K. Muller, J. N. Skepper, P. A. Midgley and M. Welland, Direct imaging of single-walled carbon nanotubes in cells, *Nat. Nanotechnol.*, 2007, **2**, 713–717.
21 C. A. Poland, R. Duffin, I. Kinloch, A. Maynard, W. A. H. Wallace, A. Seaton, V. Stone, S. Brown, W. MacNee and K. Donaldson, Carbon nanotubes introduced into the abdominal cavity of mice show asbestos-like pathogenicity in a pilot study, *Nat. Nanotechnol.*, 2008, **3**, 423–428.
22 L. A. Mitchell, F. T. Lauer, S. W. Burchiel and J. D. McDonald, Mechanisms for how inhaled multiwalled carbon nanotubes suppress systemic immune function in mice, *Nat. Nanotechnol.*, 2009, **4**, 451–456.
23 L. Ma-Hock, S. Treumann, V. Strauss, S. Brill, F. Luizi, M. Mertler, K. Wiench, A. O. Gamer, B. van Ravenzwaay and R. Landsiedel, Inhalation Toxicity of Multiwall Carbon Nanotubes in Rats Exposed for 3 Months, *Toxicol. Sci.*, 2009, **112**, 468–481.
24 J. Kolosnjaj, H. Szwarc and F. Moussa, Toxicity studies of carbon nanotubes, *Adv. Exp. Med. Biol.*, 2007, **620**, 181–204.
25 K. Yang, Y. J. Li, X. F. Tan, R. Peng and Z. Liu, Behavior and Toxicity of Graphene and Its Functionalized Derivatives in Biological Systems, *Small*, 2013, **9**, 1492–1503.
26 G. H. Zuo, W. Gu, H. P. Fang and R. H. Zhou, Carbon Nanotube Wins the Competitive Binding over Proline-Rich Motif Ligand on SH3 Domain, *J. Phys. Chem. C*, 2011, **115**, 12322–12328.
27 H. Yamawaki and N. Iwai, Cytotoxicity of water-soluble fullerene in vascular endothelial cells, *Am. J. Physiol.: Cell Physiol.*, 2006, **290**, C1495–C1502.
28 C. M. Sayes, J. D. Fortner, W. Guo, D. Lyon, A. M. Boyd, K. D. Ausman, Y. J. Tao, B. Sitharaman, L. J. Wilson, J. B. Hughes, J. L. West and V. L. Colvin, The differential cytotoxicity of water-soluble fullerenes, *Nano Lett.*, 2004, **4**, 1881–1887.
29 G. Jia, H. F. Wang, L. Yan, X. Wang, R. J. Pei, T. Yan, Y. L. Zhao and X. B. Guo, Cytotoxicity of carbon nanomaterials: Single-wall nanotube, multi-wall nanotube, and fullerene, *Environ. Sci. Technol.*, 2005, **39**, 1378–1383.
30 O. Akhavan and E. Ghaderi, Toxicity of Graphene and Graphene Oxide Nanowalls Against Bacteria, *ACS Nano*, 2010, **4**, 5731–5736.
31 C. H. Lui, L. Liu, K. F. Mak, G. W. Flynn and T. F. Heinz, Ultraflat graphene, *Nature*, 2009, **462**, 339–341.
32 F. Guinea, A. K. Geim, M. I. Katsnelson and K. S. Novoselov, Generating quantizing pseudomagnetic fields by bending graphene ribbons, *Phys. Rev. B: Condens. Matter Mater. Phys.*, 2010, **81**, 035408.
33 F. Guinea, B. Horovitz and P. Le Doussal, Gauge field induced by ripples in graphene, *Phys. Rev. B: Condens. Matter Mater. Phys.*, 2008, **77**, 205421.
34 D. H. Guo, T. Kondo, T. Machida, K. Iwatake, S. Okada and J. Nakamura, Observation of Landau levels in potassium-intercalated graphite under a zero magnetic field, *Nat. Commun.*, 2012, **3**, 1068.
35 N. Levy, S. A. Burke, K. L. Meaker, M. Panlasigui, A. Zettl, F. Guinea, A. H. C. Neto and M. F. Crommie, Strain-Induced Pseudo-Magnetic Fields Greater Than 300 Tesla in Graphene Nanobubbles, *Science*, 2010, **329**, 544–547.
36 L. Meng, W. Y. He, H. Zheng, M. X. Liu, H. Yan, W. Yan, Z. D. Chu, K. K. Bai, R. F. Dou, Y. F. Zhang, Z. F. Liu, J. C. Nie and L. He, Strain-induced one-dimensional Landau level quantization in corrugated graphene, *Phys. Rev. B: Condens. Matter Mater. Phys.*, 2013, **87**, 205405.
37 X. H. Zhao, Q. J. Ma, X. X. Wu and X. Zhu, Graphene oxide-based biosensor for sensitive fluorescence detection of DNA based on exonuclease III-aided signal amplification, *Anal. Chim. Acta*, 2012, **727**, 67–70.
38 V. M. Pereira, A. H. C. Neto, H. Y. Liang and L. Mahadevan, Geometry, Mechanics, and Electronics of Singular Structures and Wrinkles in Graphene, *Phys. Rev. Lett.*, 2010, **105**, 156603.
39 T. Chen, Y. H. Xue, A. K. Roy and L. M. Dai, Transparent and Stretchable High-Performance Supercapacitors Based on Wrinkled Graphene Electrodes, *ACS Nano*, 2014, **8**, 1039–1046.
40 B. W. Zhu, Z. Q. Niu, H. Wang, W. R. Leow, H. Wang, Y. G. Li, L. Y. Zheng, J. Wei, F. W. Huo and X. D. Chen, Microstructured Graphene Arrays for Highly Sensitive Flexible Tactile Sensors, *Small*, 2014, **10**, 3625–3631.
41 Y. Geng, P. Dalhaimer, S. S. Cai, R. Tsai, M. Tewari, T. Minko and D. E. Discher, Shape effects of filaments *versus* spherical particles in flow and drug delivery, *Nat. Nanotechnol.*, 2007, **2**, 249–255.
42 X. L. Huang, L. L. Li, T. L. Liu, N. J. Hao, H. Y. Liu, D. Chen and F. Q. Tang, The Shape Effect of Mesoporous Silica Nanoparticles on Biodistribution, Clearance, and Biocompatibility *in Vivo*, *ACS Nano*, 2011, **5**, 5390–5399.
43 T. Yu, K. Greish, L. D. McGill, A. Ray and H. Ghandehari, Influence of Geometry, Porosity, and Surface Characteristics of Silica Nanoparticles on Acute Toxicity: Their Vasculature Effect and Tolerance Threshold, *ACS Nano*, 2012, **6**, 2289–2301.
44 T. K. Chiu, J. Kubelka, R. Herbst-Irmer, W. A. Eaton, J. Hofrichter and D. R. Davies, High-resolution X-ray crystal structures of the villin headpiece subdomain, an

ultrafast folding protein, *Proc. Natl. Acad. Sci. U. S. A.*, 2005, **102**, 7517–7522.

45 A. D. MacKerell, D. Bashford, M. Bellott, R. L. Dunbrack, J. D. Evanseck, M. J. Field, S. Fischer, J. Gao, H. Guo, S. Ha, D. Joseph-McCarthy, L. Kuchnir, K. Kuczera, F. T. K. Lau, C. Mattos, S. Michnick, T. Ngo, D. T. Nguyen, B. Prodhom, W. E. Reiher, B. Roux, M. Schlenkrich, J. C. Smith, R. Stote, J. Straub, M. Watanabe, J. Wiorkiewicz-Kuczera, D. Yin and M. Karplus, All-atom empirical potential for molecular modeling and dynamics studies of proteins, *J. Phys. Chem. B*, 1998, **102**, 3586–3616.

46 Y. Duan and P. A. Kollman, Pathways to a protein folding intermediate observed in a 1-microsecond simulation in aqueous solution, *Science*, 1998, **282**, 740–744.

47 H. X. Lei, C. Wu, H. G. Liu and Y. Duan, Folding free-energy landscape of villin headpiece subdomain from molecular dynamics simulations, *Proc. Natl. Acad. Sci. U. S. A.*, 2007, **104**, 4925–4930.

48 D. E. Shaw, P. Maragakis, K. Lindorff-Larsen, S. Piana, R. O. Dror, M. P. Eastwood, J. A. Bank, J. M. Jumper, J. K. Salmon, Y. B. Shan and W. Wriggers, Atomic-Level Characterization of the Structural Dynamics of Proteins, *Science*, 2010, **330**, 341–346.

49 C. D. Snow, N. Nguyen, V. S. Pande and M. Gruebele, Absolute comparison of simulated and experimental protein-folding dynamics, *Nature*, 2002, **420**, 102–106.

50 S. K. Deng and V. Berry, Wrinkled, rippled and crumpled graphene: an overview of formation mechanism, electronic properties, and applications, *Mater. Today*, 2016, **19**, 197–212.

51 Z. H. Pan, N. Liu, L. Fu and Z. F. Liu, Wrinkle Engineering: A New Approach to Massive Graphene Nanoribbon Arrays, *J. Am. Chem. Soc.*, 2011, **133**, 17578–17581.

52 W. Wang, S. D. Yang and A. Wang, Observation of the unexpected morphology of graphene wrinkle on copper substrate, *Sci. Rep.*, 2017, **7**, 8244.

53 Y. Wang, R. Yang, Z. W. Shi, L. C. Zhang, D. X. Shi, E. Wang and G. Y. Zhang, Super-Elastic Graphene Ripples for Flexible Strain Sensors, *ACS Nano*, 2011, **5**, 3645–3650.

54 J. F. Zang, S. Ryu, N. Pugno, Q. M. Wang, Q. Tu, M. J. Buehler and X. H. Zhao, Multifunctionality and control of the crumpling and unfolding of large-area graphene, *Nat. Mater.*, 2013, **12**, 321–325.

55 G. Hummer, J. C. Rasaiah and J. P. Noworyta, Water conduction through the hydrophobic channel of a carbon nanotube, *Nature*, 2001, **414**, 188–190.

56 W. L. Jorgensen, J. Chandrasekhar, J. D. Madura, R. W. Impey and M. L. Klein, Comparison of Simple Potential Functions for Simulating Liquid Water, *J. Chem. Phys.*, 1983, **79**, 926–935.

57 B. Hess, C. Kutzner, D. van der Spoel and E. Lindahl, GROMACS 4: Algorithms for highly efficient, load-balanced, and scalable molecular simulation, *J. Chem. Theory Comput.*, 2008, **4**, 435–447.

58 B. Hess, H. Bekker, H. J. C. Berendsen and J. G. E. M. Fraaije, LINCS: A linear constraint solver for molecular simulations, *J. Comput. Chem.*, 1997, **18**, 1463–1472.

59 U. Essmann, L. Perera, M. L. Berkowitz, T. Darden, H. Lee and L. G. Pedersen, A Smooth Particle Mesh Ewald Method, *J. Chem. Phys.*, 1995, **103**, 8577–8593.

60 T. Darden, D. York and L. Pedersen, Particle Mesh Ewald – an $N\cdot\log(N)$ Method for Ewald Sums in Large Systems, *J. Chem. Phys.*, 1993, **98**, 10089–10092.

61 G. Bussi, D. Donadio and M. Parrinello, Canonical sampling through velocity rescaling, *J. Chem. Phys.*, 2007, **126**, 014101.

62 H. J. C. Berendsen, J. P. M. Postma, W. F. Vangunsteren, A. Dinola and J. R. Haak, Molecular-Dynamics with Coupling to an External Bath, *J. Chem. Phys.*, 1984, **81**, 3684–3690.

63 B. Roux, The Calculation of the Potential of Mean Force Using Computer-Simulations, *Comput. Phys. Commun.*, 1995, **91**, 275–282.

64 J. G. Kirkwood, Statistical mechanics of fluid mixtures, *J. Chem. Phys.*, 1935, **3**, 300–313.

65 J. S. Hub, B. L. de Groot and D. van der Spoel, g_wham-A Free Weighted Histogram Analysis Implementation Including Robust Error and Autocorrelation Estimates, *J. Chem. Theory Comput.*, 2010, **6**, 3713–3720.

66 B. Y. Li, Y. Z. Zhang, X. Y. Meng and R. H. Zhou, Zipper-Like Unfolding of dsDNA Caused by Graphene Wrinkles, *J. Phys. Chem. C*, 2020, **124**, 3332–3340.

67 W. Kabsch and C. Sander, Dictionary of Protein Secondary Structure – Pattern-Recognition of Hydrogen-Bonded and Geometrical Features, *Biopolymers*, 1983, **22**, 2577–2637.

68 B. Y. Li, W. F. Li, J. M. Perez-Aguilar and R. H. Zhou, Mild Binding of Protein to C_2N Monolayer Reveals Its Suitable Biocompatibility, *Small*, 2017, **13**, 1603685.